Assessment through high-fidelity simulations of a low-fidelity noise prediction tool for a vertical-axis wind turbine

Brandetti, L.; Avallone, F.; De Tavernier, D.; LeBlanc, B.P.; Ferreira, Carlos; Casalino, D.

DOI
10.1016/j.jsv.2022.117486

Publication date
2022

Document Version
Final published version

Published in
Journal of Sound and Vibration

Citation (APA)
Brandetti, L., Avallone, F., De Tavernier, D., LeBlanc, B. P., Ferreira, C., & Casalino, D. (2022). Assessment through high-fidelity simulations of a low-fidelity noise prediction tool for a vertical-axis wind turbine. *Journal of Sound and Vibration*, *547*(117486), Article 117486. https://doi.org/10.1016/j.jsv.2022.117486

Journal of Sound and Vibration 547 (2023) 117486

Contents lists available at ScienceDirect

Journal of Sound and Vibration

journal homepage: www.elsevier.com/locate/jsvi

Assessment through high-fidelity simulations of a low-fidelity noise prediction tool for a vertical-axis wind turbine

Livia Brandetti [*], Francesco Avallone, Delphine De Tavernier, Bruce LeBlanc, Carlos Simão Ferreira, Damiano Casalino

Flow Physics and Technology Department, Faculty of Aerospace Engineering, Delft University of Technology, Delft, The Netherlands

ARTICLE INFO

Keywords:
Vertical-axis wind turbine
Aerodynamic
Aeroacoustics

ABSTRACT

Vertical-axis wind turbines have the potential to be installed nearby urban areas, where noise regulations are a constraint. Accurate modelling of the far-field noise with low-order fidelity methods is essential to account for noise early in the design phase. The challenge for the vertical-axis wind turbine is the unsteady azimuthal variation of the flow over the blades, which makes the prediction of the far-field noise complex with low-fidelity methods. In this paper, the state-of-the-art of low-fidelity methods are assessed against scale-resolving high-fidelity numerical simulations of a realistic vertical-axis wind turbine carried out with the lattice-Boltzmann very large eddy simulations method. High-fidelity numerical data are validated against experimental aerodynamics data of the same vertical-axis wind turbine. The low-fidelity method is based on the actuator cylinder model coupled with semi-empirical models for airfoil-self noise and turbulence-interaction noise. Results show a good agreement between the high-fidelity simulations and the low-fidelity model at low frequencies (i.e. between 2×10^1 Hz and 1×10^2 Hz), where turbulence-interaction noise is the dominant noise source. At higher frequencies, the airfoil-self noise dominates and existing methods, based on steady airfoils, do not correctly predict noise. This paper shows that the presented low-fidelity model predicts the aerodynamics and the aeroacoustics of the turbine with an acceptable accuracy for a design stage. However, improvements are needed to better predict the far-field noise for blades in an unsteady field.

1. Introduction

Depending on the orientation of the axis of rotation, wind turbines are classified as horizontal-axis wind turbines (HAWTs) and vertical-axis wind turbines (VAWTs). The advantages of the latter are, amongst others: omni-directionality, which makes them more suitable for installation in urban areas where wind direction variations are larger because of the presence of surrounding buildings, and lower maintenance cost because the generator is located on the ground [1].

When locating a wind energy system in urban areas, it is mandatory to account for noise regulations. Two major noise sources exist for operating wind turbines: mechanical and aerodynamic. The former is caused by the dynamic response of the moving mechanical components, while the latter is generated by the interaction of the airflow with the blade [2–5]. Nowadays, the major focus is on aerodynamic noise, proving that mechanical noise has been already optimized [6].

Aerodynamic noise can be divided into Turbulence-Interaction (T-I) noise and airfoil-self noise. T-I noise occurs when incoming flow turbulence interacts with the blade leading edge [4,7]. For this aerodynamic noise source, it is essential to carefully describe the

---

[*] Corresponding author.
E-mail address: l.brandetti@tudelft.nl (L. Brandetti).

https://doi.org/10.1016/j.jsv.2022.117486
Received 12 June 2022; Received in revised form 25 October 2022; Accepted 30 November 2022

turbulent flow in terms of spectral energy content and the integral length scale of the fluctuations. For a system like a VAWT, where the impinging turbulent flow can be self-generated (i.e. wake–airfoil interaction) or due to free-stream turbulence, characterization of the turbulent wake is essential. However, no accurate model has been reported in the literature yet. As a matter of fact, by comparing the analytical results of Botha et al. [8] and Pearson [9] on the QR5 rotor, a mismatch up to 10 dB is found depending on the different correction factors applied. On the same line, Botha et al. [8] found that by increasing the intensity of the turbulent fluctuations to 10%–15% of the free-stream velocity, an increase in the overall noise up to 5 dB was obtained.

Airfoil-self noise is the noise generated by a blade in a smooth flow [3]. Depending on the flow conditions, five airfoil-self noise mechanisms can be distinguished:

1. Laminar Boundary Layer-Vortex Shedding noise (LBL-VS);
2. Turbulent Boundary Layer-Trailing Edge noise (TBL-TE);
3. Separation-Stall noise (SS);
4. Trailing Edge Blunt-Vortex Shedding noise (TEB-VS);
5. Tip noise (TP).

For HAWTs, which usually operate at high Reynolds numbers Re, (i.e. $Re \geq 5 \times 10^5$), TBL-TE noise is the most relevant noise source. TBL-TE is caused by the scattering of the turbulent pressure fluctuations convecting over the sharp trailing edge [3]. Conversely, for VAWTs, TBL-TE noise is not the primary noise source. Pearson [9] and Botha et al. [8] showed that, at low Tip-Speed Ratios (TSRs), the blades of a VAWT are subjected to dynamic stall. Under this condition, the shear layer separates, creating coherent vortices which generate tonal noise (LBL-VS) [3]. When the TSR increases, dynamic stall is less relevant, and the major source of noise is T-I noise, i.e. interaction between the turbulent near wake of a blade and the following one. Pearson [9] also demonstrated that increasing the solidity of the rotor (σ) has a similar effect as increasing TSR because the induction factor is a function of both. If small VAWTs are considered, the operating Re numbers are relatively low, (i.e $Re \leq 5 \times 10^5$), and LBL-VS noise is expected to be the major source of noise. By modelling LBL-VS noise with the Brooks, Pope and Marcolini (BPM) approach [3], Pearson observed a tonal peak in the frequency range between 1×10^3 Hz – 2×10^3 Hz for a full-scale rotor. However, this result does not match with the experimental findings of Dyne [10] because of the assumption of steady incoming flow in the BPM model.

Based on the previous observations, a low-fidelity methodology to correctly predict noise for a VAWT operating at a low Re number is not available yet. To pave the way towards a low-fidelity noise prediction tool, an assessment of the noise sources is needed. To this end, the current research investigates the aerodynamic and the aeroacoustic performance of a two-bladed H-Darrieus VAWT using a multi-fidelity numerical approach. First, Lattice-Boltzmann Very Large Eddy Simulations (LB-VLES) coupled with the Ffowcs Williams and Hawkings (FWH) integral solution are carried out. This is the first dataset presented in the literature where both the aerodynamic and the acoustic fields are retrieved using the same tool, thus allowing to link far-field noise with the unsteady aerodynamics. Then, the high-fidelity numerical results are compared with the ones obtained from a low-fidelity model, used to predict the performance of a VAWT with very low computational time such that it can be used in preliminary design stages. The comparison will assess the limitations of the adopted models and provide relevant information for their improvement.

The paper is structured as follows, Section 2 describes the geometry of the test case and the simulation settings. The adopted methodologies are discussed in Section 3. The computational set-up is validated in Section 4 by means of a grid convergence study and by comparison with experimental loading data in Section 5. Aerodynamic and acoustic results are discussed in Sections 5 and 6, respectively. The main findings are summarized in Section 7.

2. Case study

The two-bladed H-Darrieus PitchVAWT, shown in Fig. 1 and experimentally investigated by LeBlanc and Simão Ferreira [11,12], is used in this study. In order to minimize blade deflection, two horizontal struts are used for each blade and located at approximately 25% and 75% of the blade length. The blades have a NACA 0021 profile and a chord c_b equals to 7.5×10^{-2} m, while the struts have a NACA 0018 profile with a chord c_s equals to 6×10^{-2} m. The diameter D of the VAWT is equal to 1.5 m, thus resulting in a rotor solidity σ of 0.1. The span s and the height H of the VAWT are equal to 1.5 m. For this study, the blade pitch angle, β, is constant and equals to 0°. More detailed information about the design of the PitchVAWT can be found in a previous work [13].

The coordinate system used in this study is shown in Fig. 1. It is a Cartesian coordinate system with the origin at the turbine's centre.

To further help in the interpretation of the results, the blade orbit is divided in two regions:

- upwind or fore half: $0^\circ \leq \theta < 180^\circ$;
- downwind or aft half: $180^\circ \leq \theta < 360^\circ$;

with θ being the blade azimuthal position and $\theta = 90^\circ$ and 270° being respectively the most upwind and downwind positions. θ is defined with respect to blade 1, therefore blade 2 lags blade 1 by 180°.

The free-stream velocity U_∞ is 4 m/s, corresponding to a Mach number M of 1×10^{-2} and a chord-based Reynolds number Re of 8.26×10^4. The free-stream turbulence intensity I_t is set to $1\% U_\infty$, similarly as in the wind tunnel experiment. The VAWT operates at a TSR of 4, corresponding to a tip velocity V_{tip} equals to 16 m/s. The flow conditions and the VAWT operation settings are summarized in Table 1.

Due to the low Re number, boundary-layer transition to turbulence, where possible, is controlled using a zig-zag strip on both airfoil sides at $15\,\% c_b$, as in the reference experiment. The tripping has a height h of 5×10^{-4} m, an amplitude A of 2×10^{-3} m and a wavelength λ of 5×10^{-3} m (Fig. 2). The set-up specifications are summarized in Table 2.

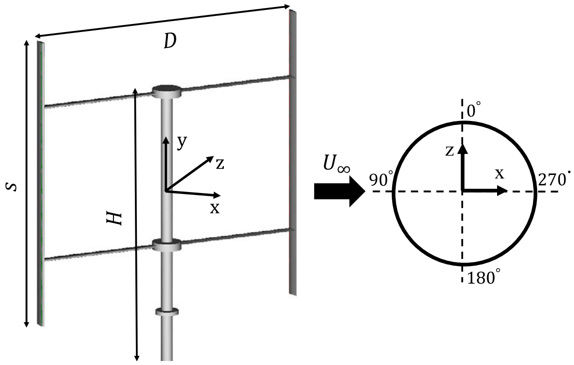

Fig. 1. PitchVAWT geometry, dimensions and coordinate system.

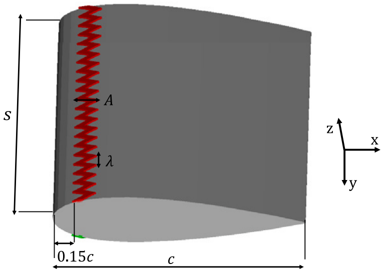

Fig. 2. Blade airfoil NACA0021 and zig-zag strip.

Table 1
Flow condition and VAWT settings.

Parameter	Value
Free-stream velocity (U_∞)	4 m/s
Tip velocity (V_{tip})	16 m/s
Tip-Speed Ratio (TSR)	4
Free-stream Mach number (M)	1×10^{-2}
Free-stream Reynolds number (Re)	8.26×10^{4}
Free-stream turbulence intensity (I_t)	$1\,\%U_\infty$

Table 2
PitchVAWT design specifications [12,13].

Parameter	Value
Number of blades (N_b)	2
Span (s)	1.5 m
Height (H)	1.5 m
Diameter (D)	1.5 m
Solidity (σ)	0.1
Blade chord (c_b)	7.5×10^{-2} m
Strut chord (c_s)	6×10^{-2} m
Blade airfoil	NACA0021
Strut airfoil	NACA0018
Blade pitch angle (β)	0°
Trip location (x_t)	$15\,\%c_b$
Trip height (h)	5×10^{-4} m
Trip amplitude (A)	2×10^{-3} m
Trip wavelength (λ)	5×10^{-3} m

3. Methodology and computational setup

3.1. High-fidelity simulations

The methodology and the computational setup used in the high-fidelity simulations are described in the following. The flow over the VAWT is computed by solving the explicit, transient, compressible LB equation, while the acoustic far field is obtained by means of the Ffowcs William and Hawkings (FWH) acoustic analogy [14].

3.1.1. Flow solver

The LB method is used to compute the flow field because it provides accurate and efficient aeroacoustic solutions for complex flow problems, as shown in previous studies in the wind energy field [15,16]. The commercial software 3DS Simulia PowerFLOW 5.5b is employed. The software solves the discrete LB equation for a finite number of directions. A detailed description of the method is out of the scope of this manuscript but the interested reader is referred to Succi [17], Shan et al. [18], and for a complete review to Chen and Doolen [19].

The LB method determines the macroscopic flow variables starting from the mesoscopic kinetic equation, i.e. the LB equation. The discretization used for this particular application consists of 19 discrete velocities in three dimensions (D3Q19), involving a third-order truncation of the Chapman–Enskog expansion. The distribution of particles is solved by means of the LB equation on a Cartesian mesh, known as a lattice. An explicit time integration and a collision model based on a unique Galilean invariant [20] are used. The equilibrium distribution function of Maxwell–Boltzmann, conventionally used for small Mach number flows, is adopted [21].

A Very Large Eddy Simulation (VLES) model is implemented to take into account the effect of the sub-grid unresolved scales of turbulence. Following Orszag and Yakhot [22], a two equation $k-\epsilon$ re-normalization group is used to compute a turbulent relaxation time that is added to the viscous relaxation time. In order to reduce the computational cost, a pressure-gradient extended wall model is used to approximate the no-slip boundary condition on solid walls [23,24]. The model is based on the extension of the generalized law-of-the-wall model [25] to take into account the effect of pressure gradient.

3.1.2. Noise computation

The compressible and time-dependent nature of the transient solution together with the low dissipation and dispersion properties of the LB scheme [26] allow the extraction of the sound pressure field directly in the near field up to a cut-off frequency corresponding to approximately 15 voxels per acoustic wavelength. In the far field, noise is computed by using the Ffowcs Williams & Hawkings [14] (FWH) equation. The formulation 1 A, developed by Farassat and Succi [27] and extended to a convective wave equation, is used in this study [26]. The formulation is implemented in the time domain using a source-time dominant algorithm [28].

3.1.3. Computational domain and boundary conditions

The simulation domain is cubic with a length of 3.7×10^2 m centred at the origin of the wind turbine reference system. At the inlet, a velocity boundary condition with a velocity equals to U_∞ is set. At the outlet, the pressure is set to the ambient pressure 1.01×10^5 Pa. At the other edges of the domain, frictionless wall boundary conditions are set. No-slip boundary conditions are applied on the VAWT. A volume of revolution is generated containing the wind turbine in a cylinder with a radial clearance of 0.4 m.

Fifteen variable resolution (VR) regions are used. The resolution increases with a factor of two from one VR region to the next. Since the main focus is the characterization of the flow around the blades, the blade path region has a higher resolution compared to the tower region (Fig. 3(a)). The finest region is defined by an offset of 1.06×10^{-3} m from the trip both on the suction side and on the pressure side to accurately capture the surface pressure fluctuations. The increase in resolution around the trip can be observed in Fig. 3(b).

An acoustic sponge is implemented by exponentially varying the kinematic viscosity per unit temperature from $5 \times 10^{-3}\ \mathrm{m}^2/\mathrm{s\ K}$ at 16 m up to $0.5\ \mathrm{m}^2/\mathrm{s\ K}$ at 47 m. This is adopted to avoid that spurious reflections from the edge of the domain contaminated the acoustic sampled data.

Simulations are seeded with the preceding simulation with a coarser grid. The flow simulation time is 2.94 s (i.e. 10 complete turbine revolutions) requiring 3.7×10^5 CPU h/revolution on a Linux Xeon E5-2690 2.9 GHz platform. The physical time step, corresponding to a Courant–Friedrichs–Lewy (CFL) number [29] of 1 in the finest mesh resolution level, is 2.06×10^{-7} s. The unsteady pressure on the surface of the VAWT is sampled with a frequency of 1×10^4 Hz for a physical time of 2.65 s (i.e. 9 complete turbine revolutions) after one transient revolution. Time-convergence has been verified as will be shown in Section 4.

3.2. Low-fidelity model

A low-fidelity model is implemented to predict the aerodynamics and the aeroacoustics of the VAWT.

The Actuator Cylinder (AC) model [30], corrected as described in Section 3.2.1, is used for the aerodynamics of the VAWT while the noise prediction methodology is based on the work of Botha et al. [8].

For the noise model, the angle of attack α and the velocity perceived by the blade V_{rel} are obtained, as described in Section 5, using three approaches: a geometric relation, the AC model and the AC model fed with blade loading data obtained from the high-fidelity simulations. These analytical models can be applied to calculate flow input parameters to be used in the low-fidelity prediction tool. This is considered acceptable for the preliminary design phase, where some inaccuracies can be tolerated. As it will be clarified in

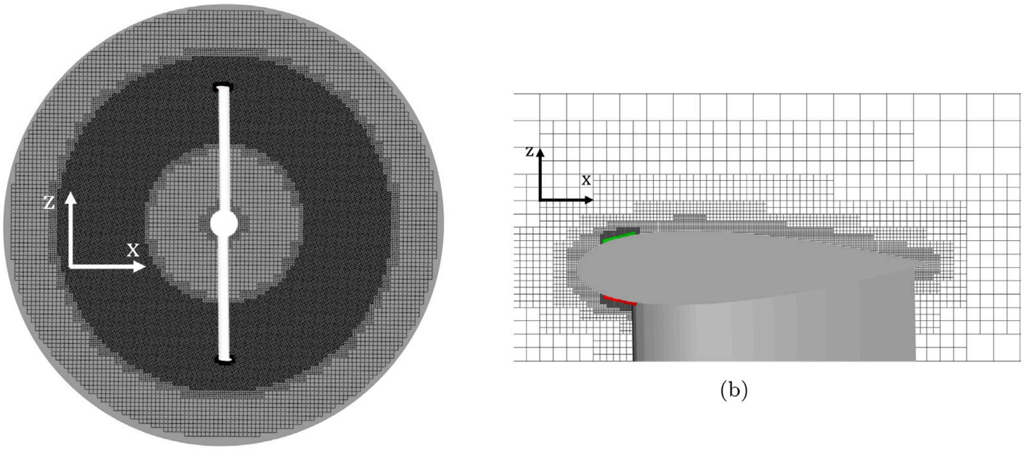

(a)

(b)

Fig. 3. Distribution of the variable resolution (VR) regions in the near field: in the local rotating reference frame (Fig. 3(a)) and around the blade, in proximity of the tip, (Fig. 3(b)). A darker colour means that the resolution is higher.

Sections 5 and 6, estimating α and V_{rel} from high-fidelity simulations is fundamental to obtain more accurate aerodynamics and aeroacoustics predictions suitable for final design analysis.

The approach of Botha et al. [8] uses a blade element approach to discretize the blades of the wind turbine. Each blade element rotates in the azimuthal direction θ. For each blade element and azimuthal position, the airfoil-self noise is estimated with the BPM model [3], while the T-I noise is modelled following the approach of Buck et al. [5]. Notice that these models are applied in a rotating coordinate system under steady flow conditions. To account for the motion of the blades with respect to the stationary observer, the Doppler correction factor is computed [31] and the spectrum at the receiver location is obtained by applying the methodology of Brooks and Burley [32].

3.2.1. Aerodynamic model

The aerodynamic forces on the VAWT are computed using the AC model developed by Madsen [30] coupled with airfoil aerodynamic data obtained from Xfoil [33]. This 2D model applies the actuator disk concept to the cylindrical actuation surface swept by the VAWT.

The reaction of the blade forces (F_n and F_t) are applied on the flow as distributed body forces (Q_n and Q_t) oriented perpendicular and tangential to the actuator surface [34]. The 2D, steady, incompressible Euler equations and the equation of continuity are solved to determine the velocity field around the AC model [35]. The induced velocities are defined as the sum of a linear solution, which is a function of the volume forces, and a non-linear solution, which is a function of the induced forces. Since the solution of the non-linear part is computationally expensive, the Mod-Lin solution is adopted [34]. Here, only the linear version of the AC model is used, and a correction factor k_a is applied to account for the non-linear part. The factor k_a is calculated from the relation between the induction factor a and the thrust coefficient C_T of the whole rotor. This relation considers that $C_T = 4a(1-a)$ for $a < 0.5$, and includes the Glauert correction for $a > 0.5$ [30]. Fig. 4 depicts the 2D AC model together with the sign convention employed in this research.

Once V_{rel} and α at each θ are known, the boundary layer integral parameters are computed with Xfoil.

Corrections applied to the aerodynamic model

Two unsteady effects characterize the VAWT's performance: dynamic stall and flow curvature. When the airfoil experiences rapid variations of the angle of attack, dynamic stall occurs. When the VAWT operates, each blade experiences a curvilinear inflow due to the rotation of the rotor. As a consequence of the flow curvature effect, V_{rel} and α vary along the chord [36]. To correctly assess the aerodynamics of the VAWT, these effects are modelled as follows:

- The Beddoes–Leishman (B–L) dynamic stall model [37] includes the effect of trailing-edge and leading-edge separation as well as the unsteady inviscid wake. The B–L model consists of four sub-models: non-linear attached flow, non-linear trailing edge separation, dynamic stall onset, vortex-induced air loads. The interested reader is referred to Leishman and Beddoes [37] for the details.
- The flow curvature effect is taken into account by assuming that the evaluation point is at three-quarters of the chord [38].

In addition, k_a is modified in the AC model, due to the heavily loaded case study (i.e. high TSR), as follows [34]:

$$k_a = \begin{cases} \frac{1}{1-a}, & a \leq 0.15 \\ \frac{1}{1-a}[0.65 + 0.35\,\exp(-4.5(a-0.15))], & a > 0.15 \end{cases}. \tag{1}$$

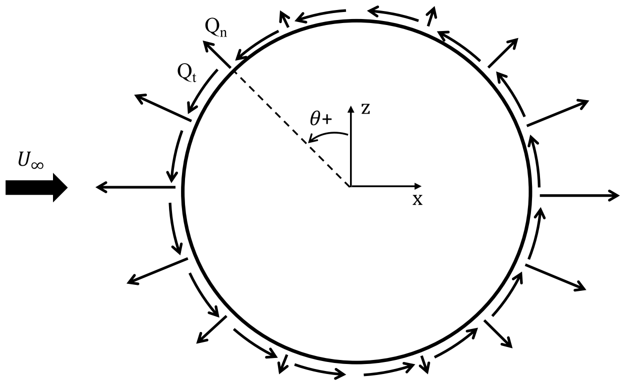

Fig. 4. 2D representation of the Actuator Cylinder (AC) model and sign convention applied.

3.2.2. Noise models

To study the acoustics of the VAWT, the noise models for the LBL-VS noise source, the TBL-TE noise source and the T-I noise source are applied.

The implemented noise models present two important limitations:

- No blade–blade interaction is considered because the blades are modelled in isolation.
- Steady, free-stream conditions under a quasi-steady time dependence are assumed.

For simplicity, only the relevant equations will be reported. The interested reader is referred to Botha et al. [8] for further information about the noise models.

Airfoil-self noise

Airfoil-self noise is generated when a steady flow interacts with a blade [3].

At low Re numbers (i.e. $Re \leq 5 \times 10^5$), Tollmien-Schlichting (T-S) waves can grow. They will generate vortex shedding, which causes tonal noise through a feedback loop. This noise generation mechanism is named LBL-VS noise and is modelled with the BPM approach [3] as follows:

$$\mathrm{SPL}_{\mathrm{LBL-VS}} = 10\log_{10}\left(\frac{\delta_p M^5 d \bar{D}_h}{r_e^2}\right) + G_1\left(\frac{St'}{St'_{\mathrm{peak}}}\right) + G_2\left[\frac{Re}{(Re)_0}\right] + G_3(\alpha), \quad (2)$$

in which $\mathrm{SPL}_{\mathrm{LBL-VS}}$ is the Sound Pressure Level in 1/3rd octave band, δ_p is the boundary layer thickness at the pressure side, d is the span-wise size of the blade element, $\bar{D}_h$ is the directivity function for the high-frequency limit, r_e is the absolute distance to the receiver and $(Re)_0$ is the chord-based Reynolds number at $\alpha = 0°$. For details on the Strouhal contributions, St' and St'_{peak}, and on the empirical functions, G_1, G_2 and G_3, the reader can refer to Brooks et al. [3].

At high Re number (i.e. $Re \geq 5 \times 10^5$), TBL develops over the airfoil. Because of the surface discontinuity at the trailing edge, the surface pressure fluctuations beneath the TBL are scattered as noise. This noise generation mechanism is named TBL-TE. The SPL in 1/3rd octave band for the TBL-TE noise ($\mathrm{SPL}_{\mathrm{TBL-TE}}$) is obtained as the sum of three contributions: one from the attached TBL at the pressure side (SPL_p), one from the attached TBL at the suction side (SPL_s) and one that accounts for the separated boundary layer at high α (SPL_α):

$$\mathrm{SPL}_{\mathrm{TBL-TE}} = 10\log_{10}\left|10^{\left(\frac{\mathrm{SPL}_p}{10}\right)} + 10^{\left(\frac{\mathrm{SPL}_s}{10}\right)} + 10^{\left(\frac{\mathrm{SPL}_\alpha}{10}\right)}\right|. \quad (3)$$

For $\alpha \leq 12.5°$, the terms in Eq. (3) are:

$$\mathrm{SPL}_p = 10\log_{10}\left(\frac{\delta_p^* M^5 d \bar{D}_h}{r_e^2}\right) + A\left(\frac{St_p}{St_1}\right) + (K_1 - 3) + \Delta K_1, \quad (4)$$

$$\mathrm{SPL}_s = 10\log_{10}\left(\frac{\delta_s^* M^5 d \bar{D}_h}{r_e^2}\right) + A\left(\frac{St_s}{St_1}\right) + (K_1 - 3), \quad (5)$$

$$\mathrm{SPL}_\alpha = 10\log_{10}\left(\frac{\delta_s^* M^5 d \bar{D}_h}{r_e^2}\right) + B\left(\frac{St_s}{St_2}\right) + (K_2), \quad (6)$$

while for $\alpha \geq 12.5°$

$$\mathrm{SPL}_p = -\infty, \quad (7)$$

$$\mathrm{SPL}_s = -\infty, \tag{8}$$

$$\mathrm{SPL}_\alpha = 10\log_{10}\left(\frac{\delta_s^* M^5 d \bar{D}_l}{r_e^2}\right) + A'\left(\frac{St_s}{St_2}\right) + (K_2), \tag{9}$$

in which δ_p^* and δ_s^* are the boundary layer displacement thickness at the pressure side and at the suction side, respectively and $\bar{D}_l$ is the directivity function for the low-frequency limit. The Strouhal contributions, St_p, St_s, St_1 and St_2, the empirical functions, A, A' and B, and the amplitude correction factors, K_1, K_2 and ΔK_1, can be found in [3].

Notice that the boundary layer parameters used in the BPM model are determined analytically. For the detailed equations, the interested reader is referred to Brooks et al. [3].

In the work of Botha et al. [8], the airfoil-self noise is also predicted with the iTNO model [39] (i.e. an improved version of the TNO model developed by Blake [40] and Parchen [41]). This model is found to provide accurate noise predictions for non-symmetric airfoil at high wind speed. However, the separation-stall noise is not modelled. For this reason and for the fact that the PitchVAWT has symmetric airfoils and operates at low wind speeds, the iTNO model is not applied in the current study.

Turbulence-interaction noise

T-I noise is produced when inflow turbulence impinges on the blade leading edge [4]. Different models have been proposed in the literature such as the one of Paterson and Amiet [2] and the one of Buck et al. [5]. Both methodologies compute the SPL of the T-I noise ($\mathrm{SPL}_{\mathrm{inflow}}$) as the sum of the high-frequency and low-frequency components of the noise:

$$\mathrm{SPL}_{\mathrm{inflow}} = \mathrm{SPL}^H_{\mathrm{inflow}} + 10\log_{10}\left(\frac{\mathrm{LFC}}{1+\mathrm{LFC}}\right), \tag{10}$$

in which LFC is the blending function introduced by Lowson and Ollerhead [42] and Moriarty and Migliore [43].

On the other hand, the high-frequency component, $\mathrm{SPL}^H_{\mathrm{inflow}}$, is different. For the model of Paterson and Amiet [2], the incoming turbulence is defined with the von Kármán spectrum while for the one of Buck et al. [5] the turbulence length scale is substituted with the turbulence dissipation rate ε by applying the Kolmogorov spectrum [44]. The value of ε is estimated with the relationship from Taylor [45] as:

$$\varepsilon = c_\varepsilon \frac{k_t^{3/2}}{L_t}, \tag{11}$$

in which $c_\varepsilon = 5.5\times10^{-1}$ is a constant selected to match the high-frequency asymptote of the Buck model to that of the Paterson and Amiet model, k_t is the turbulent kinetic energy derived from the root mean square turbulent fluctuations as the product between the turbulence intensity at the inlet and the velocity perceived by the blade and $L_t = 7.5\times10^{-3}$ m is the integral length scale of turbulence at the airfoil inlet.

This modification leads to less complex calculations and to short measurement times. However, Botha et al. [8] demonstrates that the two models predict the same noise spectrum. Therefore, the model of Buck et al. [5] is preferred. The sound pressure level $\mathrm{SPL}^H_{\mathrm{inflow,B}}$ is:

$$\mathrm{SPL}^H_{\mathrm{inflow,B}} = 10\log_{10}\left[\frac{\rho_\infty^2 c_0^2 d}{2r_e^2} M^3 \varepsilon^{(2/3)} k^{-(5/3)} \bar{D}_{\mathrm{LE}}\right] + 77.6, \tag{12}$$

where ρ_∞ is the free-stream density, c_0 is the sound speed, k is the wave-number ($k = (2\pi f)/V_{\mathrm{rel}}$) and $\bar{D}_{\mathrm{LE}}$ is the directivity function for the low-frequency limit computed at the leading edge.

4. Assessment of the high-fidelity numerical simulations

A grid resolution study is performed for the high-fidelity numerical simulations to verify that the solution does not vary with the computational grid. High-fidelity numerical simulations with three grid resolutions are carried out. For the three cases, the most refined region (i.e., around the blade) has 3×10^2 (coarse), 4.24×10^2 (medium) and 6×10^2 (fine) voxels per VAWT chord. This is achieved by proportionally increasing the resolution of each refinement region. The corresponding number of fine equivalent voxels N for the three configurations is 1.9×10^7, 3.6×10^7 and 6.9×10^7.

The time-averaged thrust coefficient C_T, defined as in Eq. (13), the Power Spectral Density (PSD), expressed as dB/Hz, and the Overall Sound Pressure Level (OASPL) of far-field acoustic pressure, indicated in dB using a reference pressure of 2×10^{-5} Pa, are used as integral parameters for the convergence analysis.

$$C_T = \frac{T}{\frac{1}{2}\rho_\infty U_\infty^2 A_{\mathrm{rot}}}, \tag{13}$$

In Eq. (13), T is the time-averaged thrust (i.e. the force along inflow direction, generated by the VAWT) and A_{rot} is the rotor frontal area, which is equal to $(D\times s)$.

The C_T is plotted in Fig. 5 for the three grid resolutions, where N is the number of fine equivalent voxels. In the same figure, data from the AC models are reported as constant C_T values. Results from the AC model are plotted using polars obtained from

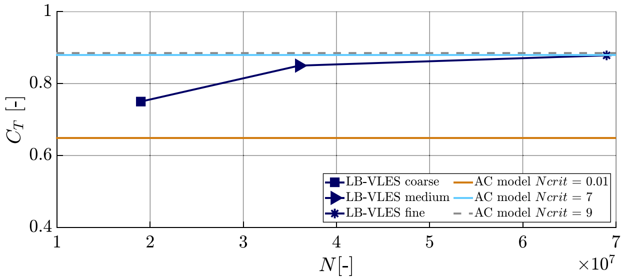

Fig. 5. The time-averaged thrust coefficient C_T versus the number of fine equivalent voxels N. The LB-VLES results are compared with results from AC model with aerodynamic polars obtained using $Ncrit$ equal to 0.01, 7 and 9.

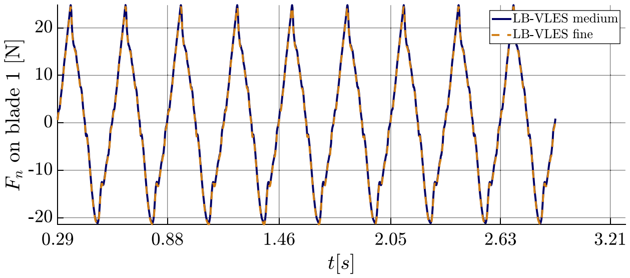

Fig. 6. Time–history of the normal force component on a single blade F_n. The LB-VLES results with medium resolution are compared with the LB-VLES results with fine resolution.

Xfoil with $Ncrit$ equal to 0.01, 7 and 9 to stress the strong dependence of the results from the aerodynamic polars used as input. Note that $Ncrit$ is used in solver as Xfoil to determine the transition location. It is based on the e^N theory, which states that the transition occurs roughly when linear theory predicts that an initial disturbance has grown by a factor of e^N [33]. The choice of using a range of polars instead of only using the polar with the zig-zag strip was motivated by the poor performance of Xfoil at low Reynolds numbers. Specifically, $Ncrit = 0.01$ represents the case of a fully turbulent flow, where the transition is amplified just after the linear instability begins. Minor variations between the low-fidelity data with $Ncrit = 7$ and with $Ncrit = 9$ can be observed in Fig. 5. Results show convergence for the fine simulation case and very good agreement with the low-fidelity data with $Ncrit = 7$ (or $Ncrit = 9$).

Time-convergence for the LB-VLES simulation is also demonstrated with a time–history of the normal force component on a single blade F_n in Fig. 6. Simulation results are plotted after one transient revolution and show a good agreement between the medium and the fine resolution.

Acoustic data are obtained on two circular arrays of equally spaced virtual microphones placed at $2.6D$ from the centre of the VAWT. The angular spacing between the microphones is 10°. One array with 27 microphones is in the x-y plane (Fig. 7(a)), while the other with 36 microphones is in the x-z plane (Fig. 7(b)).

In Figs. 8 and 9, the PSD as a function of frequency f and the OASPL directivity patterns are plotted to ensure that also far-field noise data converge. The far-field noise is computed using the FWH acoustic analogy as described in Section 3.1.2. PSD is shown for two microphones at $\theta = 0°$ and at $\phi = 0°$, respectively. For the PSD, the maximum difference between the two finest grids is $2\,\mathrm{dB/Hz}$ for $\theta = 0°$. For the low grid resolution, an overestimation of the OASPL for angles in the range $100° < \phi < 300°$ and $135° < \theta < 315°$ is found and corresponds to $1.5\,\mathrm{dB}$. In overall, results show a good agreement between the medium resolution and the fine resolution, confirming that the fine simulation case has reached convergence also from an acoustic point of view. Based on these results, the fine simulation will be used in the following.

5. Flow field description and aerodynamic performance

Flow field description

A detailed analysis of the complex aerodynamic flow features is reported using data from high-fidelity simulations. This description is essential to understand the limitations of the low-fidelity methodology in predicting the VAWT's aerodynamic performance.

An instantaneous flow field at $\theta = 90°$ is shown in Fig. 10 through iso-surfaces of the λ_2 criterion for vortex identification, colour-contoured with the non-dimensional velocity magnitude $\underline{V}/U_\infty$. The figure illustrates that most of the vortices in the near wake of each blade are generated at the tip and the struts. While at the tip, the vortices are coherent and have a large scale, in the proximity of the struts, they show a smaller scale already in the near wake.

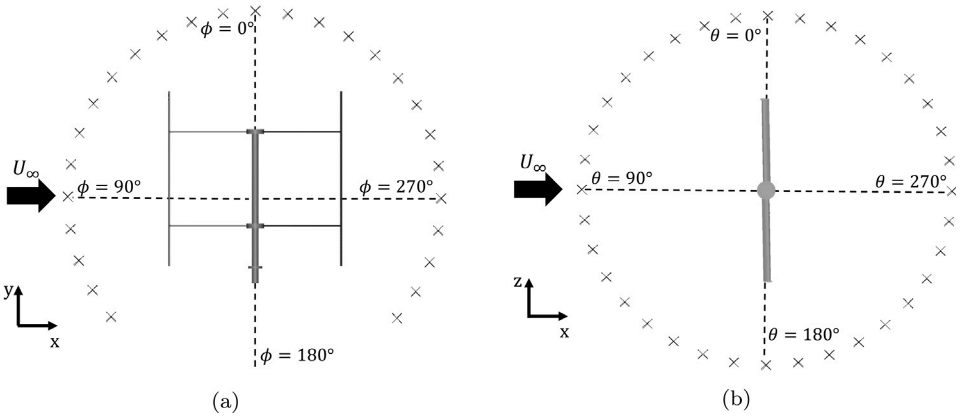

(a)

(b)

Fig. 7. Two circular arrays of equally spaced virtual microphones placed at 2.6D from the centre of the VAWT: array with 27 microphones in the x-y plane (Fig. 7(a)) and array with 36 microphones in the x-z plane (Fig. 7(b)).

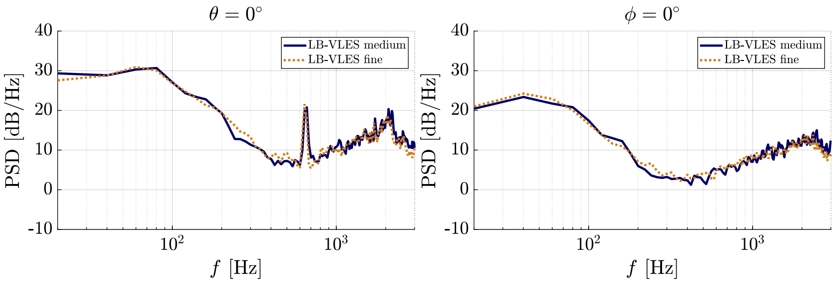

Fig. 8. Power Spectral Density PSD versus frequency f for two microphones placed at 2.6D from the centre of the VAWT: $\theta = 0°$ (left-side) and $\phi = 0°$ (right-side). The LB-VLES results with medium resolution are compared with the LB-VLES results with fine resolution.

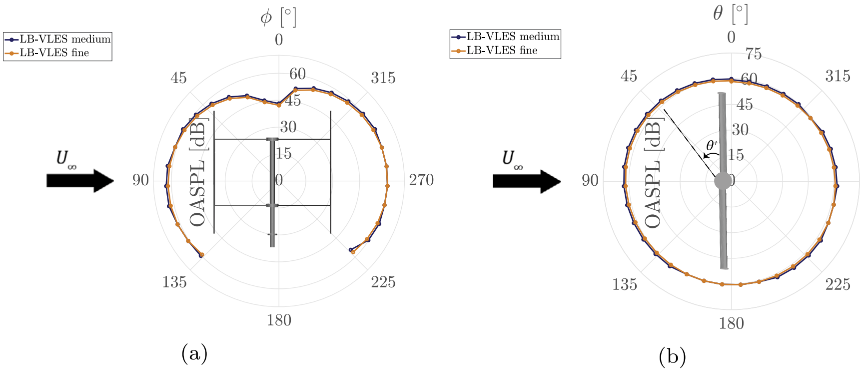

(a)

(b)

Fig. 9. Directivity plots of the Overall Sound Pressure Level (OASPL) computed on: a circular array of 27 microphones in the x-y plane (Fig. 9(a)) and on a circular array of 36 microphones in the x-z plane (Fig. 9(b)). The LB-VLES results with medium resolution are compared with the LB-VLES results with fine resolution.

Because of the presence of these structures, each blade is subjected to both Blade-Wake Interaction (BWI) and Blade-Vortex Interaction (BVI) [46]. These phenomena are better shown in Fig. 11, where non-dimensional vorticity magnitude $\omega/(V_{\text{tip}}/c)$ is plotted at two planes: at the tip (sub-figures 1 and 2) and in correspondence of the upper struts (sub-figures 3 and 4). For each plane, the blades are at two azimuthal positions as annotated in the figures.

In the absence of the struts, the vorticity is mostly shed when the blade is located at $\theta = 0°$. This is expected because the derivative of the loading is the largest in this position. Conversely, where the struts are present, the vorticity is strongly shed at all the azimuthal positions. The interaction between the two blades is clearly visible in sub-figure 3, where the trailing edge shed vorticity of the blade in $\theta = 180°$ interacts with the leading edge of the blade in $\theta = 0°$. The vorticity is spread in the field and does not interact with the leading edge of the blade in $\theta = 270°$.

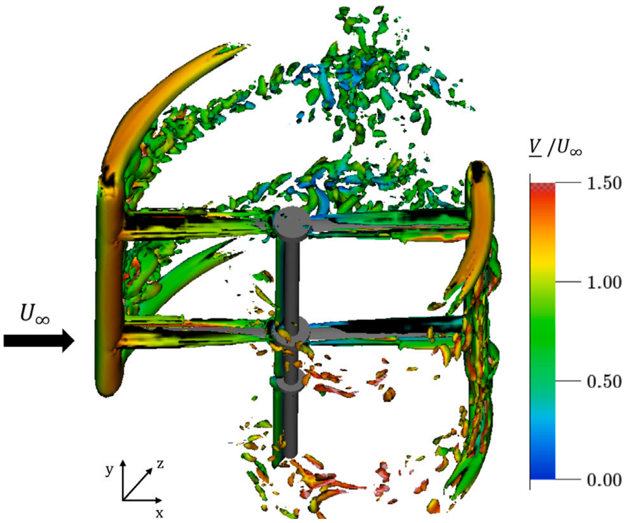

Fig. 10. View of the instantaneous flow field at $\theta = 90°$ visualized through the λ_2 criterion for vortex visualization colour contoured with the non-dimensional velocity magnitude $\underline{V}/U_\infty$. (For interpretation of the references to colour in this figure legend, the reader is referred to the web version of this article.)

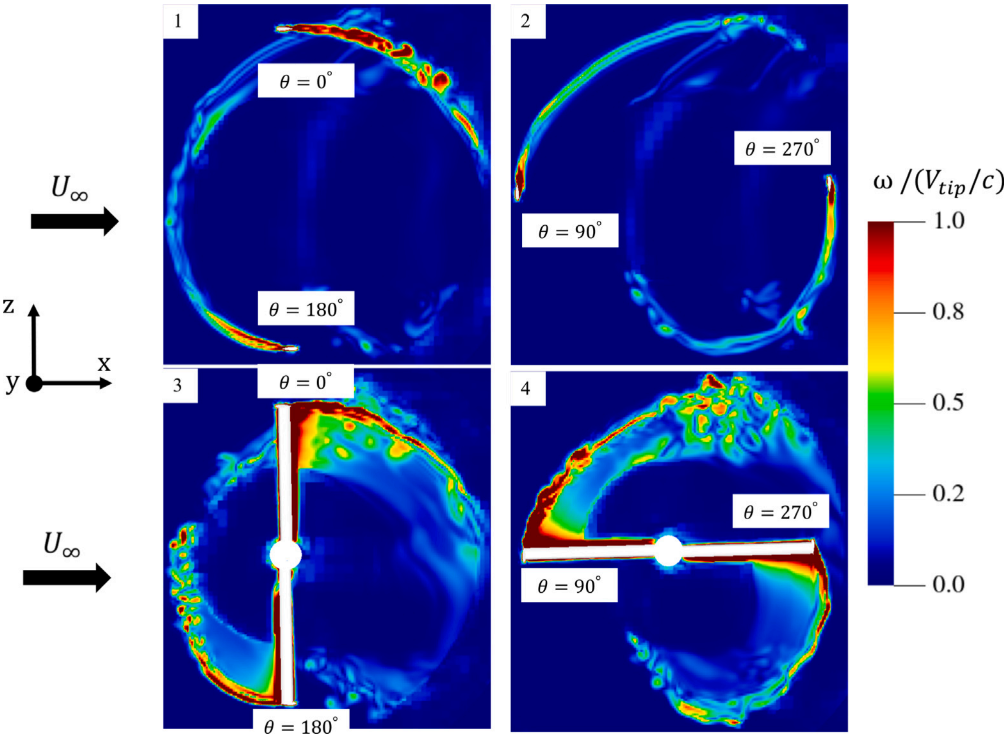

Fig. 11. Instantaneous flow field visualized through the non-dimensional vorticity magnitude $\omega/(V_{\mathrm{tip}}/c)$. Sub-figures 1 and 2: plane at the tip. Sub-figures 3 and 4: plane at the upper struts.

Another important aspect, that needs to be taken into account to properly model the aerodynamics of VAWTs with low-fidelity methods, is the unsteady flow field to which each blade section is subjected during one rotation.

An inherent effect of this unsteadiness is flow separation, which is investigated in Fig. 12. Here, contours of the non-dimensional stream-wise velocity u/U_∞ at the mid plane are plotted for blade 1 at four θ: 50°, 90°, 220° and 270°. As it can be observed, the contours look discrete because of downsampling of the numerical results. At $\theta = 50°$, the flow is attached up to 50% of the blade chord where separation starts. Conversely for $\theta = 90°$, the most upwind location, separation starts at 20% of the blade chord. At $\theta = 220°$, no flow separation is found in the high-fidelity simulations; separation is again visible at $\theta = 270°$. At this location, the

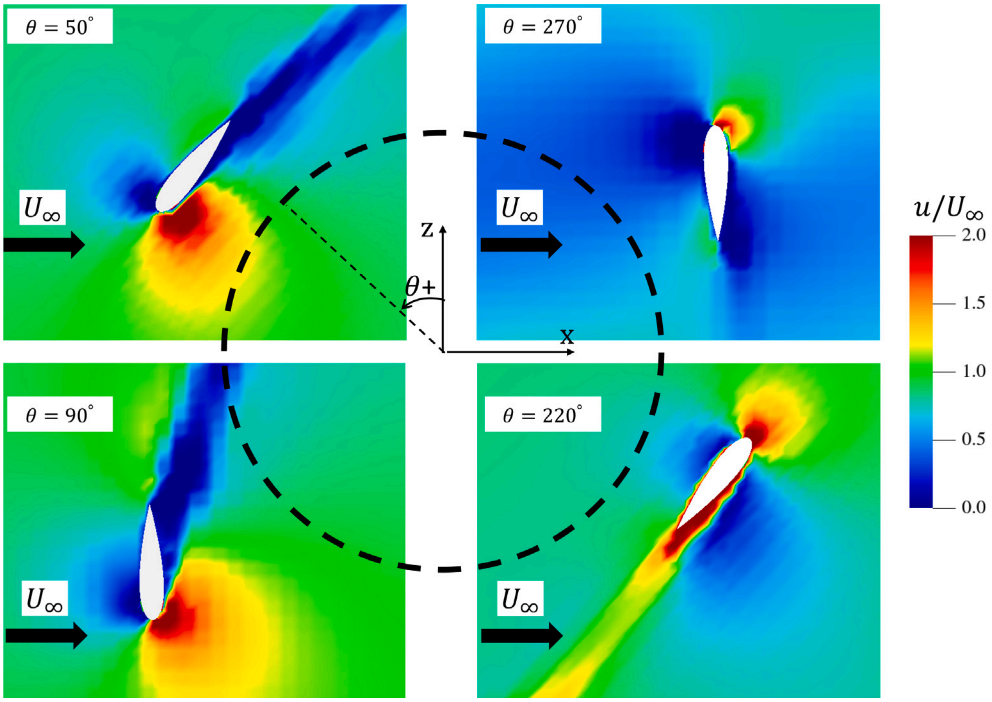

Fig. 12. Instantaneous non-dimensional stream-wise velocity u/U_∞ at the mid plane for four azimuthal positions θ of blade 1: 50°, 90°, 220°, 270°. The rotating system of reference is used.

blade passes through a region with velocity deficit caused by the downstream wake of the tower, which has a significant effect on the flow over the blade [47] and on the acoustics of the turbine (Section 6). The qualitative description given from visual inspections of the figures is confirmed by the distributions of the pressure coefficient C_p over blade 1, which are not shown for the sake of conciseness.

Aerodynamic performance

The phase-locked normal force component on a single blade F_n is shown in Fig. 13. The LB-VLES forces are obtained from a phase-locked average over 9 rotations; the experimental forces are obtained from a phase-locked average out of approximately 200 data points per azimuthal location. The experimental loading data, presented both for clean blades and tripped blades, are measured using a set of strain gauges on the top strut of blade 1. A full-bridge strain gauge setup is utilized in an axial configuration to compensate for any vertical bending or temperature fluctuations which can occur while testing [12,48]. Azimuthal locations, where experimental data have a poor signal-to-noise ratio, are not plotted. Results from AC model are only presented for two extreme polars (i.e. $Ncrit = 0.01$ and $Ncrit = 7$) because results with $Ncrit = 9$ are very similar to those obtained with $Ncrit = 7$. It is important to mention that the loads from the LB-VLES simulation and the experiment are averaged over the rotor span, including 3D tip effects and vortex shedding. These 3D effects are not considered in the low-fidelity method due to its 2D formulation.

Overall a good agreement between the methodologies is found both in terms of trends and absolute values. All methods correctly predict the F_n at $\theta = 0°$. For $15° < \theta < 48°$ and $200° < \theta < 220°$, the LB-VLES show good agreement with the two experimental dataset, while at $\theta = 90°$ and $\theta = 270°$ the LB-VLES results agree better with the clean experimental data. This is because the zig-zag strip, used in the high-fidelity numerical simulation, is not effective at those angles, as shown in the previous figures. Even if this can be solved by increasing the size of the zig-zag strip in the high fidelity numerical simulation, this would result in additional unwanted noise sources and over-tripping in a range of angles of attack. The figure further shows that, upwind for $0° < \theta < 180°$, the AC model results strongly depend on the polar used. Downwind, for $180° < \theta < 360°$, differences are mainly attributed to the inaccurate prediction of the induction and to wake effects (3D) in the low-fidelity method.

A challenge for low-fidelity methods is to accurately predict the dynamic of α and V_{rel}, which vary with θ [49]. In the following, α and V_{rel} are obtained with three approaches: through a geometric relation, from the AC model and using the blade loads from the high-fidelity simulations as inputs for the AC model. The latter approach has been applied because there is no agreed formulation on how to extract α and V_{rel} from high-fidelity simulations [8,50]. Details on the methodology to compute α and V_{rel} from high-fidelity normal blade loads are beyond the scope of the paper, and the interested reader is referred to the literature [51]. No experimental data for α and V_{rel} are available.

The ones given by the geometric relation are shown in Eqs. (14) and (15), under the assumption of a constant V_{rot} and U_∞.

$$\alpha = \arctan\left(\frac{\sin(\theta)}{\cos(\theta) + \mathrm{TSR}}\right) + p, \tag{14}$$

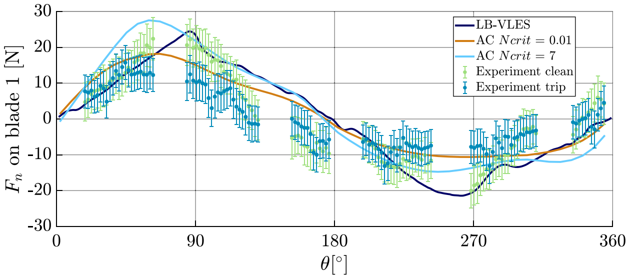

Fig. 13. Phase-locked normal force on blade 1 F_n versus the azimuthal angle θ during one turbine rotation. The LB-VLES results are compared with experimental data and results from AC model with two extreme polars ($Ncrit = 0.01$ and $Ncrit = 7$).

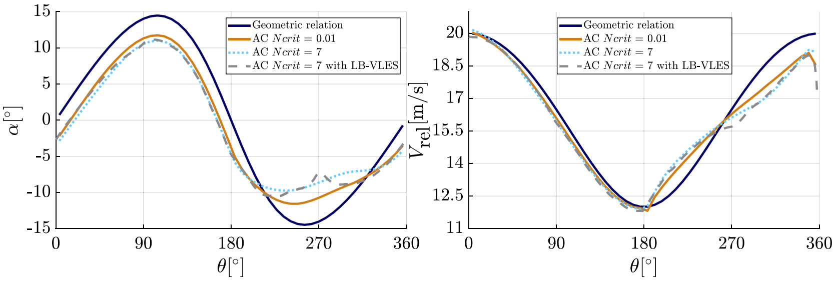

Fig. 14. Angle of attack α (left-side) and perceived velocity V_{rel} (right-side) versus azimuthal angle θ during one turbine rotation. The geometric relation results are compared with the results from AC model ($Ncrit = 0.01$ and $Ncrit = 7$) and AC model with $Ncrit = 7$ feed with LB-VLES blade load data.

$$V_{\text{rel}} = U_\infty \sqrt{1 + 2\ \text{TSR} \cos(\theta) + \text{TSR}^2}, \tag{15}$$

where p is the fixed pitch angle of the airfoil.

For the AC model, α and V_{rel} are determined with Eqs. (16) and (17).

$$\alpha = \arctan\left(\frac{V_n}{V_t}\right) - p, \tag{16}$$

$$V_{\text{rel}} = \sqrt{V_n^2 + V_t^2}. \tag{17}$$

V_n and V_t are the normal and the tangential relative wind speed with respect to the AC, defined as:

$$V_n = V_x \sin\theta - V_z \cos\theta, \tag{18}$$

$$V_t = V_x \cos\theta + V_z \sin\theta + V_{\text{rot}}. \tag{19}$$

with $V_x = U_\infty(1 + w_x)$ and $V_z = U_\infty w_z$ the components in x- and z- directions of the velocity, respectively, w_x is the x-induction and w_z is the z-induction.

Both α and V_{rel}, computed with the three approaches, are plotted in Fig. 14. Results obtained using the geometric relation show the most relevant differences between all the methodologies. This is because the induction is not considered. For the other approaches, α has a sinusoidal shape in the turbine fore half, while a flat shaped aft half. This is due to fact that the flow is significantly affected by the blade passage in the fore aft [52]. The differences between the other approaches are smaller and it is evident the minor impact of using high-fidelity blade loads inputs in the AC model.

6. Acoustics

6.1. Comparison between low-fidelity methodologies

To demonstrate the effect of α and V_{rel} on the acoustic predictions, results from the noise model with α and V_{rel} predicted with the geometric relation and results from the noise model with α and V_{rel} predicted with the AC model for $Ncrit = 0.01$ and $Ncrit = 7$ are compared in Figs. 15 and 16 as SPL versus frequency f. The SPL is expressed in dB and is evaluated at $2.6D$ from the centre of the VAWT in the x-z plane, specifically at $\theta = 90°$ and at $\theta = 270°$. The methodology has been described in Section 3.2.2.

By looking at the different SPL spectra, it is clear that the most dominant noise sources are: T-I noise below 7×10^1 Hz, TBL-TE noise from 7×10^1 Hz to 3×10^2 Hz and LBL-VS noise from 3×10^2 Hz to 8×10^2 Hz.

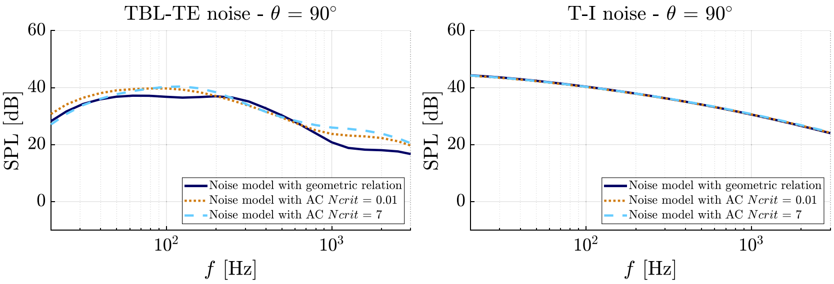

Fig. 15. Sound Pressure Level SPL versus frequency f. The noise model with geometric relation inputs results are compared with results from the noise model with AC data for two extreme polars ($Ncrit = 0.01$ and $Ncrit = 7$).

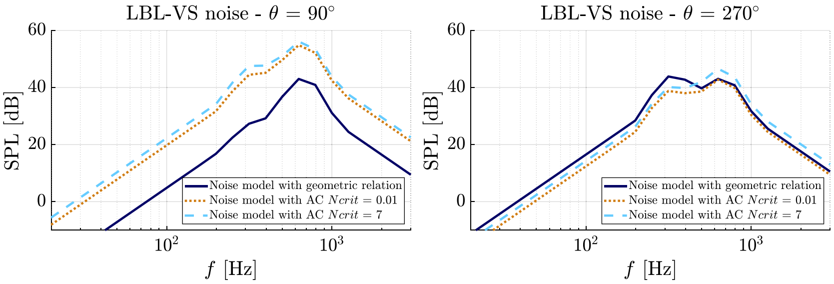

Fig. 16. Sound Pressure Level SPL versus frequency f. The noise model with geometric relation inputs results are compared with results from the noise model with AC data for two extreme polars ($Ncrit = 0.01$ and $Ncrit = 7$).

For the T-I noise, a good agreement between the models is found both in terms of trends and absolute values. This is because the Buck model only depends on V_{rel} (Eq. (12)), which is very similar for the three models at $\theta = 90°$ (Fig. (14)). For the TBL-TE noise, results using the geometric relation show the most relevant differences between all the methods because of the largest difference in α (Fig. (14)).

The effect of a different α on the SPL is clearly visible in the LBL-VS noise spectra. This is due to the fact that an α-dependent function is used to model the LBL-VS noise (Eq. (2)).

6.2. Comparison between LB-VLES and noise model with aerodynamic data from the AC model

The comparison between LB-VLES data and low-fidelity data in Section 5 has shown the limitations of the low-fidelity methodologies in the prediction of the VAWT's aerodynamics. In the following, the effect of these limitations on the acoustic prediction will be investigated by comparing the LB-VLES results with the results from the noise model with aerodynamic inputs from the AC with $Ncrit = 7$. Aerodynamic inputs from the other low-fidelity models are not considered due to their inaccurate flow modelling. No experimental acoustic data is available for the comparison.

Fig. 17 illustrates the directivity plots of the OASPL on the two circular microphone arrays (Fig. 7). The OASPL is expressed in dB with reference pressure equal to 2×10^{-5} Pa. Data are integrated between one Blade Passing Frequency (BPF) and 20 BPF, where the BPF equals 6.8 Hz.

An overall good agreement between the methodologies is found in terms of trends. The resulting acoustic field is slightly asymmetric as expected from the flow dynamics of the VAWT. The main differences in the absolute values are attributed, for the microphones located in the x-y plane, to the incoming wind speed and to 3D effects while, for the microphones located in the x-z plane, to the non correct prediction of α and V_{rel}.

The previous observations are further supported by the SPL spectra in Figs. 18 to 20. Two microphones in the x-y plane and four microphones in the x-z plane are used: $\phi = 20°$, $\phi = 270°$, $\theta = 50°$, $\theta = 90°$, $\theta = 220°$ and $\theta = 270°$.

In the figures, results from the low-fidelity method are plotted for each noise generation mechanisms. The tonal loading noise is not modelled because for this case study, in real-life, the rotational frequency is low and out of the audible range.

At $\phi = 20°$, good agreement between LB-VLES and the results from the low-fidelity models is found. The two methods confirm the dominance of the T-I noise at low frequency as well as the dominance of the TBL-TE noise at medium frequency. The small differences in the tonal peak of the LBL-VS at 6×10^2 Hz are attributed to 3D vortex-shedding effects, which represent one of the limitation of the low-fidelity methodology.

At $\phi = 270°$, the acoustic predictions of the noise model are strongly affected by the presence of the struts and of the tower (Section 5).

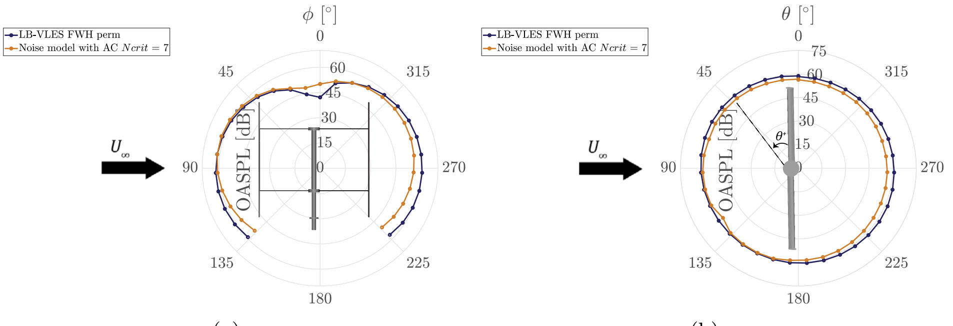

(a) (b)

Fig. 17. Directivity plots of the Overall Sound Pressure Level (OASPL) computed on: a circular array of 27 microphones in the x-y plane (Fig. 17(a)) and on a circular array of 36 microphones in the x-z plane (Fig. 17(b)). The LB-VLES results are compared with results from the noise model with AC data for $Ncrit$ =7.

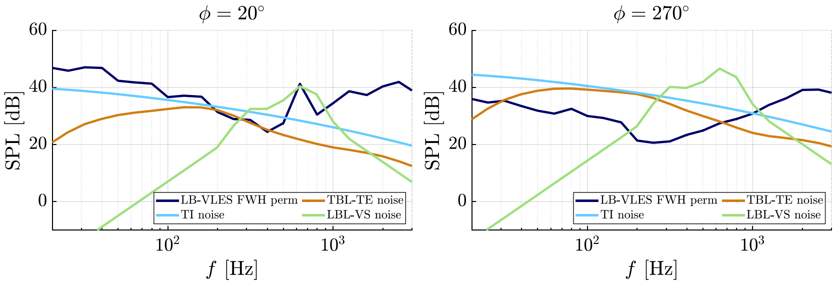

Fig. 18. Sound Pressure Level SPL versus frequency f obtained from two microphones in the x-y plane: at $\phi = 20°$ (left-side) and at $\phi = 270°$ (right-side). The LB-VLES results are compared with results from the noise model with AC data for $Ncrit$ = 7.

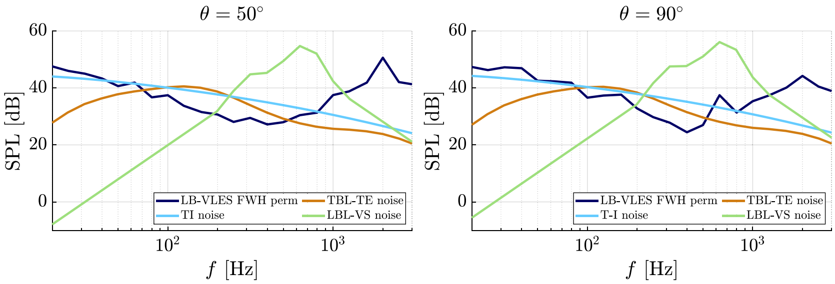

Fig. 19. Sound Pressure Level SPL versus frequency f obtained from two microphones in the x-z plane: at θ = 50° (left-side) and at θ = 90° (right-side). The LB-VLES results are compared with results from the noise model with AC data for $Ncrit$ = 7.

At θ = 50°, 90° and 220° and below 1×10^2 Hz, the differences between the LB-VLES and the noise model are small and it is evident the relevance of T-I noise.

At θ = 270°, the noise model predicts lower levels of T-I noise with respect to the LB-VLES. This is due to tower shadow, as illustrated in Fig. 12. The consequent velocity deficit causes laminar flow over larger portions of the airfoil which is reflected in the LBL-VS peak at 6×10^2 Hz [3]. At $\theta = 90°$, the increasing angle of attack caused by flow separation (Fig. 12), leads to a decrease in the predicted LBL-VS peak by the LB-VLES [3]. The low-fidelity model does not capture this effect due to an inaccurate prediction of α and V_{rel}.

Overall, no agreement in the absolute value for the TBL-TE noise is found for two reasons. First, the low-fidelity model does not account for BVI and BWI because the blades are modelled as isolated [8]. Second, the model assumes steady flow conditions and the occurrence of flow separation only when $\alpha > 12.5°$ [9,53]. This condition is demonstrated to be not true for the case under study (Section 5).

To further demonstrate the influence of the struts and the tower and the occurrence of 3D effects and blade-wake interactions, visualizations of the instantaneous noise contribution from each solid surface at a given microphone location is computed with $Opty\partial B$-PFNOISESCAN [54]. The resulting unsteady surface field is Fourier transformed and then visualized in different integration bands as SPL/m^2.

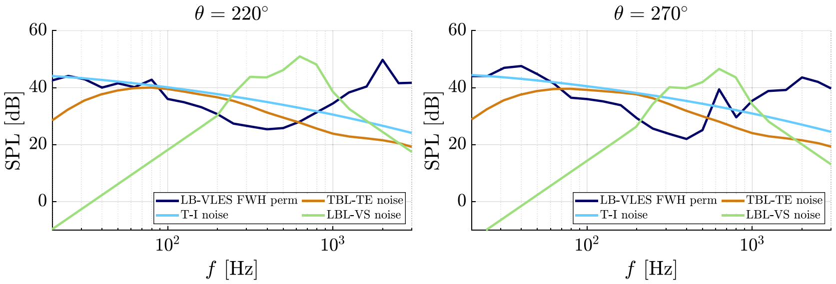

Fig. 20. Sound Pressure Level SPL versus frequency f obtained from two microphones in the x-z plane: at $\theta = 220°$ (left-side) and at $\theta = 270°$ (right-side). The LB-VLES results are compared with results from the noise model with AC data for $Ncrit = 7$.

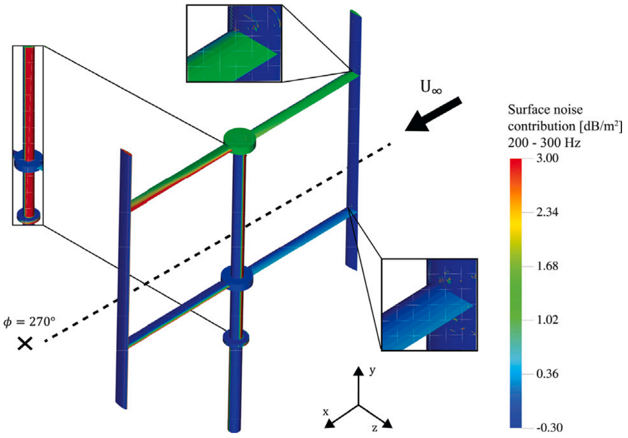

Fig. 21. FWH integral contribution from a microphone in the x-y plane at $\phi = 270°$.

Figs. 21 to 23 illustrate the noise source maps computed by using three different microphones: $\phi = 270°$, $\theta = 50°$ and $\theta = 90°$. Since in the comparison of the SPL spectra, the noise models show to inaccurately predict the TBL-TE noise and the LBL-VS noise, the corresponding frequency range are used in the analysis: 2×10^2 Hz–3×10^2 Hz and 5×10^2 Hz–6×10^2 Hz.

At $\phi = 270°$, the struts and the tower are detected as the main noise sources, while the blades present lower noise contributions. This explains the trend observed in the SPL spectrum (Fig. 18), where the low-fidelity model predicts higher noise levels for not modelling the struts and the tower.

The influence of 3D phenomena on the overall noise contribution is evident at $\theta = 50°$. Vortices are visible at the tip and the bottom of the blade, while 3D effects generate from junction flows in the proximity of strut-blade connections. For this reason, the assumptions about the 2D flow and related radiated noise are not valid, resulting in lower noise levels of the LB-VLES with respect to the one predicted by the low-fidelity model between 2×10^2 Hz and 3×10^2 Hz (Fig. 19).

At $\theta = 90°$, the noise source map reveals the dominance of the most upwind blade because it experiences higher flow velocity and angle of attack. As above-mentioned, from 5×10^2 Hz to 6×10^2 Hz, the increase in the angle of attack causes a decrease in the LBL-VS peak predicted by the LB-VLES (Fig. 19). Another cause of the lower noise contribution of the most downwind blade is attributed to BVI and BWI, proving that the assumption of modelling blade as isolated is not true for VAWT [53].

7. Conclusions

This study assesses of the state-of-the-art of a low-fidelity noise prediction tool for a VAWT operating at a low Re number. The two-bladed H-Darrieus PitchVAWT geometry is used, for which experimental aerodynamic data are available. The limitations of the low-fidelity methodology are investigated through a comparison with high-fidelity data. This dataset allows to study the relation between the aerodynamics and the aeroacoustics of the VAWT.

Upwind, the results from the AC model strongly depends on the aerodynamic polars used as input because of the complex flow dynamic of airfoils at low Re number [55]. The influence of the polars confirms how a correct prediction of the flow is essential to predict the aerodynamics of the VAWT correctly.

Downwind, differences in trend are found due to the inaccurate prediction of α and V_{rel}. These parameters cannot be correctly computed because 3D effects, blade–blade interactions, flow separation and tower shadow are not included in the low-fidelity model. The occurrence of 3D effects at the tip and the struts as well as BVI and BWI is demonstrated with three-dimensional

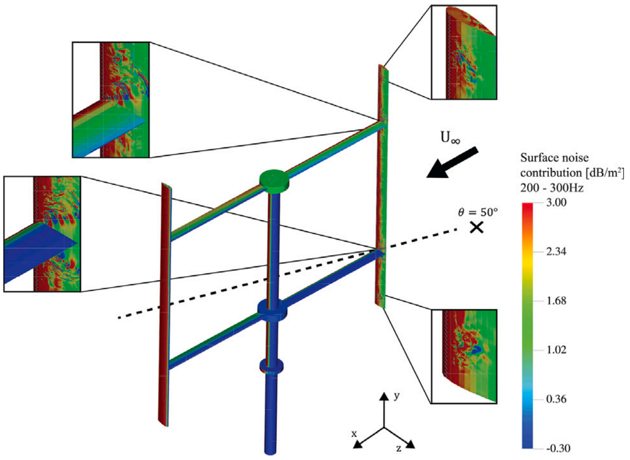

Fig. 22. FWH integral contribution from a microphone in the x-z plane at $\theta = 50°$.

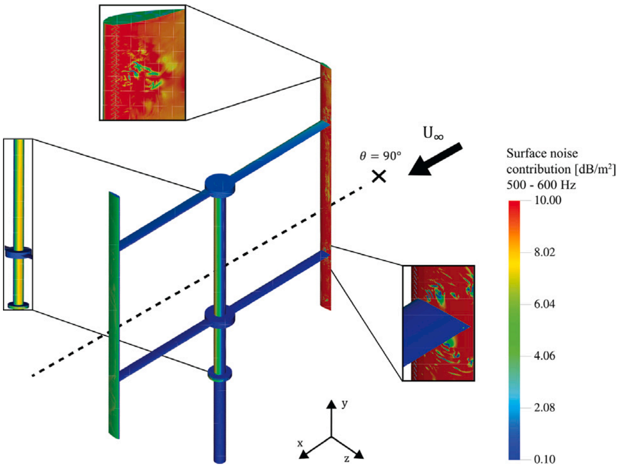

Fig. 23. FWH integral contribution from a microphone in the x-z plane at $\theta = 90°$.

flow visualization through the λ_2 criterion and contour of the instantaneous vorticity magnitude. Contours of the instantaneous stream-wise velocity component also demonstrate flow separation and tower shadow, which enhance the unsteady flow field.

These aerodynamic limitations are reflected in the directivity patterns and in the SPLs. The Buck model is proven to accurately predict the T-I noise in the absence of tower shadow. Due to the inaccurate prediction of α and V_{rel} and the assumption of steady flow, the TBL-TE noise and the LBL-VS noise are not correctly modelled with the BPM approach. However, the applications of the model themselves are reasonable since input parameters are varied in a quasi-steady way during the rotations. Overall, from the comparison between the low-fidelity prediction tool and the high-fidelity ones, it is found that they predict the aerodynamics and the aeroacoustics of a VAWT with acceptable accuracy for a preliminary design stage.

In future studies, the low-fidelity prediction tool will be improved as follows:

- Extracting α and V_{rel} from the high-fidelity simulations.
- Recomputing the polars employed in the AC model by using the corrected values of α along the rotation.
- Estimating the noise emitted by the blades by applying these corrected inputs.
- Including the aerodynamic estimation of the struts by extending the AC model to the Actuator-in-Actuator cylinder (AC-squared) model, described in [56] and further applied to a rotor with inclined struts in Chapter 7 of De Tavernier [57].
- Including the aeroacoustics estimation of the struts by extending the approach of Botha et al. [8] to consider the horizontal rotation of the struts.
- Performing high-fidelity simulations of the isolated blade and strut to further compare against the analytical models.

With the considered improvements, 3D effects, blade–blade interactions, flow separation, presence of the struts and tower shadow will be included in the low-fidelity prediction tool allowing a more accurate estimation of the aerodynamics and the aeroacoustics of a VAWT for final design stages.

CRediT authorship contribution statement

Livia Brandetti: Conceptualization, Methodology, Software, Validation, Investigation, Visualization, Writing - original draft. **Francesco Avallone:** Conceptualization, Methodology, Supervision, Investigation, Writing - review and editing. **Delphine De Tavernier:** Methodology, Writing - review. **Bruce LeBlanc:** Experimental data and the CAD of the turbine. **Carlos Simão Ferreira:** Conceptualization. **Damiano Casalino:** Conceptualization, Methodology, Writing - review.

Declaration of competing interest

The authors declare that they have no known competing financial interests or personal relationships that could have appeared to influence the work reported in this paper.

Acknowledgments

This research is part of the Arkom-Tulyp Wind project and is sponsored by RVO, The Netherlands, the Netherlands Enterprise Agency, under a Hernieuwbare Energie (Sustainable Energy) subsidy. All authors read and approved the manuscript.

References

[1] S. Eriksson, H. Bernhoff, M. Leijon, Evaluation of different turbine concepts for wind power, Renew. Sustain. Energy Rev. 12 (2008) 1419–1434, http://dx.doi.org/10.1016/j.rser.2006.05.017.

[2] R. Paterson, R. Amiet, Noise and surface pressure response of an airfoil to incident turbulence, J. Aircr. 14 (8) (1977) 729–736.

[3] T.F. Brooks, S. Pope, M.A. Marcolini, Airfoil Self-Noise and Prediction, NASA Reference Publication 1218, 1989, pp. 1–142, http://dx.doi.org/10.1080/09524622.2008.9753825, URL: http://ntrs.nasa.gov/archive/nasa/casi.ntrs.nasa.gov/19890016302.pdf.

[4] A.L. Rogers, J.F. Manwell, S. Wright, Wind Turbine Acoustic Noise, Technical Report, 2006, http://dx.doi.org/10.1260/0957456042872777.

[5] S. Buck, S. Oerlemans, S. Palo, Experimental characterization of turbulent inflow noise on a full-scale wind turbine, J. Sound Vib. 385 (2016) 219–238.

[6] S. Wagner, R. Bareiss, G. Guidati, Wind Turbine Noise, Springer Verlag, 1996.

[7] J.W. Kim, S. Haeri, P.F. Joseph, On the reduction of aerofoil-turbulence interaction noise associated with wavy leading edges, J. Fluid Mech. 792 (2016) 526–552.

[8] J.D.M. Botha, A. Shahroki, H. Rice, An implementation of an aeroacoustic prediction model for broadband noise from a vertical axis wind turbine using a CFD informed methodology, J. Sound Vib. 410 (2017) 389–415, http://dx.doi.org/10.1016/j.jsv.2017.08.038.

[9] C. Pearson, Vertical Axis Wind Turbine Acoustics (Ph.D. thesis), Corpus Christi College Cambridge University, 2013.

[10] B.K. Dyne, Wind Turbine Noise Measurements, Technical Report, Southampton, 2007.

[11] B. LeBlanc, C. Simão Ferreira, Experimental determination of thrust loading of a 2-bladed vertical axis wind turbine, J. Phys. Conf. Ser. 1037 (2) (2018) http://dx.doi.org/10.1088/1742-6596/1037/2/022043.

[12] B. LeBlanc, C. Simão Ferreira, Estimation of blade loads for a variable pitch vertical axis wind turbine from particle image velocimetry, Wind Energy (2021) 1–20, http://dx.doi.org/10.1002/we.2674.

[13] B. LeBlanc, C. Simão Ferreira, Overview and design of PitchVAWT : Vertical axis wind turbine with active variable pitch for experimental and numerical comparison, in: 2018 Wind Energy Symposium, Kissimmee, Florida, 2018, pp. 1–11.

[14] J.E. Ffowcs Williams, D.L. Hawkings, Sound generation by turbulence and surfaces in arbitray motion, Philos. Trans. R. Soc. Lond. Ser. A 264 (1151) (1969) 321–342.

[15] F. Avallone, D. Ragni, D. Casalino, On the effect of the tip-clearance ratio on the aeroacoustics of a diffuser-augmented wind turbine, Renew. Energy 152 (2020) 1317–1327, http://dx.doi.org/10.1016/j.renene.2020.01.064.

[16] V. Dighe, F. Avallone, G. van Bussel, Effects of yawed inflow on the aerodynamic and aeroacoustic performance of ducted wind turbines, J. Wind Eng. Ind. Aerodyn. 201 (2020) 104174, http://dx.doi.org/10.1016/j.jweia.2020.104174.

[17] S. Succi, The Lattice Boltzmann Equation, first ed., Claredon Press, Oxford, 2001.

[18] X. Shan, X.F. Yuan, H. Chen, Kinetic theory representation of hydrodynamics: a way behond the Navier-Stokes equation, J. Fluid Mech. 550 (2006) 413–441, http://dx.doi.org/10.1017/S0022112005008153.

[19] S. Chen, G.D. Doolen, Lattice Boltzmann method for fluid flows, Annu. Rev. Fluid Mech. 30 (1) (1998) 329–364, http://dx.doi.org/10.1146/annurev.fluid.30.1.329.

[20] H. Chen, R. Zhang, P. Gopalakrishnan, Lattice Boltzmann collision operatos enforcing isotropy and Galilean invariance, 2015.

[21] H. Chen, S. Chen, W.H. Matthaeus, Recovery of the Navier-Stokes equations using a lattice-gas Boltzmann method, Phys. Rev. A 45 (8) (1992) 5339–5342, http://dx.doi.org/10.1103/PhysRevA.45.R5339.

[22] S.A. Orszag, V. Yakhot, Renormalization group analysis of turbulence, in: Proceedings of the International Congress of Mathematicians, Vol. 1, 1987, pp. 1395–1399.

[23] C.M. Teixeria, Incorporating turbulence models into the lattice-boltzmann method, third ed., Internat. J. Modern Phys. C 9 (8) (1998) 1159–1175.

[24] D. Wilcox, Turbulence Modeling for CFD, third ed., DCW Industries, Incorporated, 2006.

[25] B. Launder, D. Spalding, The numerical computation of turbulent flow computer methods, Comput. Methods Appl. Mech. Engrg. 3 (1974) 269–289, http://dx.doi.org/10.1016/0045-7825(74)90029-2.

[26] G.A. Bres, F. Perot, D.M. Freed, Properties of the Lattice – Boltzmann method for acoustics, in: 15th AIAA/CEAS Aeroacoustic Conference, 2009, pp. 2009–3711.

[27] F. Farassat, G. Succi, A review of propeller discrete frequency noise prediction technology with emphasis on two current methods for time domain calculations, J. Sound Vib. 71 (3) (1980) 399–419.

[28] D. Casalino, An advanced time approach for acoustic analogy predictions, J. Sound Vib. 261 (2003) 583–612.

[29] R. Courant, K. Friedrichs, H. Lewy, On the partial difference equations of mathematical physics, IBM J. Res. Dev. 11 (2) (1967) 215–234.

[30] H.A. Madsen, The Actuator Cylinder - A Flow Model for Vertical Axis Wind Turbines (Ph.D. thesis), Aalborg University Centre, 1982, http://dx.doi.org/10.13140/RG.2.1.2512.3040.

[31] G. Ruijgrok, Elements of aviation acoustics, ISBN: 90-6275-899-1, 1993, p. 309.

[32] T.F. Brooks, C.L. Burley, Rotor broadband noise prediction with comparison to model data, J. the American Helicopter Society 49 (1) (2004) 28–42.

[33] M. Drela, M.B. Gilest, Viscous-inviscid analysis of transonic and low Reynolds number airfoils, AIAA J. 25 (10) (1987) 1347–1355, URL: https://doi.org/10.2514/3.9789.

[34] H.A. Madsen, T.J. Larsen, U.S. Paulsen, L. Vita, Implementation of the actuator cylinder flow model in the HAWC2 code for aeroelastic simulations on vertical axis wind turbines, in: 51st AIAA Aerospace Sciences Meeting Including the New Horizons Forum and Aerospace Exposition, 2013, pp. 1–12, http://dx.doi.org/10.2514/6.2013-913.

[35] J. Katz, A. Plotkin, Low-Speed Aerodynamics, second ed., Cambridge University Press, 2001.

[36] P. Migliore, W. Wolfe, J. Fanucci, Flow curvature effects on darrieus turbine blade aerodynamics, J. Energy 4 (2) (1980) 49–55, http://dx.doi.org/10.2514/3.62459.

[37] J. Leishman, T. Beddoes, A semi-empirical model for dynamic stall, J. Am. Helicopter Soc 34 (3) (1989) 3–17, http://dx.doi.org/10.4050/JAHS.34.3.3.

[38] A. Li, Double Actuator Cylinder (AC) Model of a Tandem Vertical- Axis Wind Turbine (VAWT) Counter-Rotating Rotor Concept, Technical Report, 2017.

[39] S. Lee, Source characterization of turbulent boundary layer trailing edge noise using an improved TNO model, in: Aeroacoustics Conference, American Institute of Aeroacoustics and Astronautics, Lyon, France, 2016, pp. 1–28, http://dx.doi.org/10.2514/6.2016-2812.

[40] W. Blake, Mechanics of Flow-Induced Sound and Vibration, Vol. 2, 2017, p. 694.

[41] R. Parchen, Progress report DRAW: a prediction scheme for trailing-edge noise based on detailed boundary-layer characteristics, TNO institute of Applied Physics, 1998.

[42] M.V. Lowson, J.B. Ollerhead, A theoretical study of helicopter noise, J. Sound Vib. 9 (2) (1969) 197–222.

[43] P. Moriarty, P. Migliore, Semi-Empirical Aeroacoustic Noise Prediction Code for Wind Turbines, Technical Report, National Renewable Energy Laboratory, Golden, CO, 2003.

[44] P.A. Davidson, Turbulence: An Introduction for Scientists and Engineers, Oxford Uni ed., Oxford, UK, 2004.

[45] G.I. Taylor, Statistical theory of turbulence, in: Proceedings of the Royal Society of London. Series a, Mathematical and Physical Sciences, 1935, pp. 421–444.

[46] G. Tescione, On the Aerodynamics of a Vertical Axis Wind Turbine Wake: An Experimental and Numerical Study (Ph.D. thesis), Delft University of Technology, 2016, http://dx.doi.org/10.4233/uuid.

[47] C. Noyes, C. Qin, E. Loth, S. Schreck, Measurements and predictions of wind turbine tower shadow and fairing effects, J. Wind Eng. Ind. Aerodyn. 179 (2018) 297–307, http://dx.doi.org/10.1016/j.jweia.2018.06.012, URL: http://www.sciencedirect.com/science/article/pii/S0167610518301065.

[48] B. LeBlanc, C. Simão Ferreira, Estimation of blade loads for a variable pitch vertical axis wind turbine with strain gage measurements, Wind Energy (2022) 1–16, http://dx.doi.org/10.1002/we.2713.

[49] C. Simão Ferreira, G. van Kuik, G. van Bussel, F. Scarano, Visualization by PIV of dynamic stall on a vertical axis wind turbine, Exp. Fluids (46) (2009) 97–108, http://dx.doi.org/10.1007/s00348-008-0543-z.

[50] P.F. Melani, F. Balduzzi, L. Brandetti, C. Simão Ferreira, A. Bianchini, An experimental and numerical analysis of the dynamic variation of the angle of attack in a vertical-axis wind turbine, J. Phys. Conf. Ser. 1618 (5) (2020) http://dx.doi.org/10.1088/1742-6596/1618/5/052064.

[51] P.F. Melani, F. Balduzzi, G. Ferrara, A. Bianchini, How to extract the angle attack on airfoils in cycloidal motion from a flow field solved with computational fluid dynamics? Development and verification of a robust computational procedure, Energy Convers. Manage. 223 (2020) 113284, http://dx.doi.org/10.1016/j.enconman.2020.113284.

[52] A. Rezaeiha, H. Montazeri, B. Blocken, Characterization of aerodynamic performance of vertical axis wind turbines : Impact of operational parameters, Energy Convers. Manage. 169 (2018) 45–77, http://dx.doi.org/10.1016/j.enconman.2018.05.042.

[53] W.R. Graham, C.E. Pearson, Noise from a model-scale vertical-axis wind turbine, AIAA J. 60 (1) (2022) 224–235, http://dx.doi.org/10.2514/1.J060531.

[54] D. Casalino, E. Grande, G. Romani, D. Ragni, F. Avallone, Definition of a benchmark for low Reynolds number propeller aeroacoustics, Aerosp. Sci. Technol. 113 (2021) 106707, http://dx.doi.org/10.1016/j.ast.2021.106707.

[55] W.L. Traub, Experimental investigation of the effect of trip strips at low Reynolds number, J. Aircr. 48 (5) (2011) 1776–1784, http://dx.doi.org/10.2514/1.C031375.

[56] D. De Tavernier, C. Simão Ferreira, An extended actuator cylinder model : Actuator-in-actuator cylinder (AC-squared) model, Wind Energy (2019) 1–13, http://dx.doi.org/10.1002/we.2340.

[57] D. De Tavernier, Aerodynamic Advances in Vertical-Axis Wind Turbines (Ph.D. thesis), 2021.